Point Defect Engineering: Co-Doping Synergy Realizing Superior Performance in n-Type Bi_2Te_3 Thermoelectric Materials

Bin Zhu, Wu Wang, Juan Cui, and Jiaqing He*

Bi_2Te_3 has attracted great attention because of its excellent thermoelectric (TE) performance around room temperature. However, the TE property of the n-type Bi_2Te_3 is still relatively low compared to the p-type counterpart, which seriously hinders its commercial application with a combination of the n-type and p-type materials. Herein, an effective process of Cl and W co-doping is employed into the n-type Bi_2Te_3 materials to enhance its TE properties. The $Bi_{1.996}W_{0.004}Te_{2.476}Cl_{0.024}Se_{0.5}$ sample achieves a peak and average ZT over 1.3 and 1.2, respectively, at temperature range of 300–575 K. A 24-leg TE module of this n-type material and a home-made p-type Bi_2Te_3 sample can produce a high efficiency over 6% at a temperature gradient of 235 K, which possesses a 71% improvement compared with a commercial Bi_2Te_3 module. This high performance is ascribed to the effect of the Cl and W doping. This co-doping not only significantly increases the Grüneisen parameter but also successfully induces interstitial atoms in the van der Waals gap, which lead to a low lattice thermal conductivity (κ_l) of 0.31 W m^{-1} K^{-1} and a boosted charge transport. This finding represents an important step to promote the development of the n-type Bi_2Te_3 materials.

1. Introduction

Thermoelectric (TE) materials have attracted increasing attention due to the ability to convert heat into electricity or vice versa. Generally, the efficiency of energy conversion of a TE device is determined by the dimensionless figure of merit ZT, which is regarded as $S^2\sigma T/\kappa$ (S, σ, T, and κ are the Seebeck coefficient, electrical conductivity, absolute temperature, and thermal conductivity, respectively).[1] In the past decade, although many high-performance TE materials with ingenious process have been reported, such as SnSe,[2] GeTe,[3] Mg_3Sb_2, and PbS,[4] they are limited in the applications because of their poor mechanical properties, high costs, or non-stability performance. The Bi_2Te_3-based system is still the only commercial TE material for room temperature application.

Dr. B. Zhu, Dr. W. Wang, Dr. J. Cui, Prof. J. He
Shenzhen Key Laboratory of Thermoelectric Materials
Department of Physics
and Guangdong Provincial Key Laboratory of Energy Materials
for Electric Power
Southern University of Science and Technology
Shenzhen 518055, China
E-mail: hejq@sustech.edu.cn

Recently, p-type polycrystalline Bi_2Te_3-based alloy has been carefully investigated. For example, the samples fabricated by liquid phase sintering showed a high ZT of 1.86, which is a very high value in room temperature TE materials.[5] Moreover, powders are fabricated through different post treatment processes, such as melt spinning (MS) or ball milling (BM), followed with the hot pressing (HP) or spark plasma sintering (SPS), to decrease lattice thermal conductivity. The peak ZT of 1.3–1.5 was obtained below 400 K, which is not suitable for power generation.[6] To solve this problem, a tiny amount of Ca has been doped into $Bi_{0.5}Sb_{1.5}Te_3$ alloy, and the optimal temperature range has been shifted over 400 K.[7] Besides, other dopants, such as Cu, Ag, and Zn, have all been demonstrated to effectively enhance electrical properties in p-type polycrystalline B_2Te_3-based alloys; high ZTs over 1.5 have been reported in many studies.[8] Considerable effort has also been made to enhance the TE properties of n-type Bi_2Te_3 as well. Although suitable dopants and delicate fabrication methods are proposed, the lattice thermal conductivity at room temperature is still over 0.4 W m^{-1} K^{-1}, and peak ZT is ≈1.2 below 400 K.[9]

Herein, we proposed a technique to enhance the TE performance of n-type Bi_2Te_3 material by introducing special point defects (**Figure 1**a). The W_{Bi} and Cl_{Te} were employed to provide electrons to optimize the electrical properties of Bi_2Te_3 material. W exists as $(WCl_2)^{4+}$ during the WCl_6 doping due to the high oxidation for W^{6+},[10] which would generate interstitial defect Te_i, as shown in the Figure 1b. These interstitial atoms not only scatter high frequency phonons as a kind of point defect, but also enlarge van der Waals gap in a large area to enhance the anharmonicity, which scatter whole frequency phonons and thus largely reduces the κ_l to ≈0.31 W m^{-1} K^{-1}. As a result, the peak and average ZT of over 1.3 and ≈1.2 was achieved in $Bi_{1.996}W_{0.004}Te_{2.476}Cl_{0.024}Se_{0.5}$ sample at a temperature range of 300–575 K, which is higher than most reported n-type Bi_2Te_3-based bulk materials, as shown in Figure 1c.[9,11] Moreover, a TE module made of $Bi_{1.996}W_{0.004}Te_{2.476}Cl_{0.024}Se_{0.5}$ sample n-legs and homemade $Bi_{0.5}Sb_{1.5}Te_3$ p-legs was fabricated. A high efficiency of over 6% was obtained at a temperature difference (ΔT) of 235 K, as shown in the Figure 1d. Only our previous work showed a slightly higher performance, but the fabrication process is apparently complex.[8c,d,12] In this work, we only used traditional melting combined with SPS process, avoiding
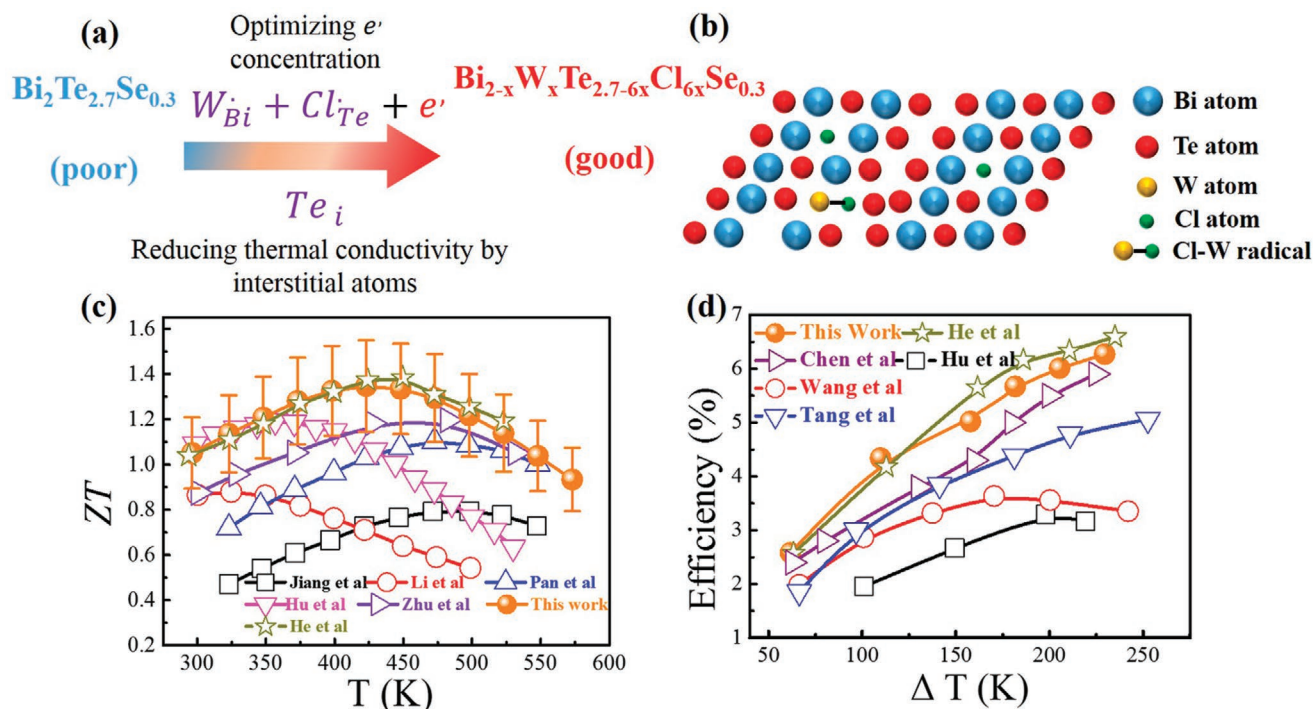
Figure 1. a) Point defects engineering process for enhancing TE performance of n-type Bi_2Te_3-based alloys, b) schematic of the generation of interstitial atoms, c) reported ZT values of n-type Bi_2Te_3-based alloys,[9,11] d) energy conversion efficiency of the 24-leg TE module in this work, and a comparison of reported values of Bi_2Te_3-based TE modules in the literature.[8c,d,11e,12]

the influence of mechanical deformation in point defect. The contribution of different point defects was analyzed. The high performances in materials and device indicate that our strategy is useful for enhancing the TE properties of n-type polycrystalline Bi_2Te_3 materials, and it will speed up the application of TE materials.

2. Results and Discussion

$Bi_{2-x}W_xTe_{2.5-6x}Cl_{6x}Se_{0.5}$ ($x = 0.001$–0.007) samples were fabricated by sealed silica tube melting method. The as-obtained samples after SPS were hand milled to powders for X-ray diffraction (XRD) analysis, as shown in the Figure S2a, Supporting Information. The XRD data were normalized and matched with the standard phase of $Bi_2Te_{2.5}Se_{0.5}$, in which no impurity peak was found. But it should be noted that the peaks in XRD patterns shift to high angle with increasing of W and Cl content (Figure S2b, Supporting Information) and indicate the lattice parameter shrinks of samples, which could ascribe to the smaller atomic radius of W and Cl. Although the texturing degree calculated from the XRD data is relatively low (about 0.05), we still measured the TE performance in both the in-pane and out-of-plane directions (the measuring direction has been illustrated in Figure S3, Supporting Information) as shown in Figures S4, Supporting Information, due to the anisotropic nature of Bi_2Te_3-based alloy. These results reveal that the ZT value along the in-plane direction was much higher than the out-of-plane direction. Therefore, the TE data along the in-plane direction of our samples is only discussed in the

main text. Figure S1, Supporting Information, and **Figure 2** present the electrical properties of pristine and co-doped samples. The TE data of pristine sample has been illustrated in the Figure S1, Supporting Information. The Seebeck coefficient (S) of the pristine $Bi_2Te_{2.5}Se_{0.5}$ sample shows a p–n transition near 425 K (Figure S1, Supporting Information), while all co-doped samples have complete n-type conduction in the whole measured temperature range (Figure 2). With Cl and W content increasing, the σ sharply increased to the 2200 S cm^{-1} at room temperature in $0.007WCl_6$ sample, which is almost three-fold higher than that of the $0.001WCl_6$ sample (Figure 2a). This could be attributed to the Cl and W co-doping, which introduced electrons as shown in Figure 2c. The S shows a very unusual trend presented in Figure 2b. With increasing doping content, the S increased at first and then decreased. The point of inflection was at the 0.004 sample with the highest value of -195 µV K^{-1} at 500 K. Therefore, the power factor (PF) of the 0.003 and 0.004 samples in Figure 2d increased dramatically to ≈ 40 µW cm^{-1} K^{-2} at 300 K, which was about 2.7-fold higher than that of the 0.001 sample. To understand this unusual phenomenon in the S, we calculated the effective mass by Single Parabolic Band (SPB) model. As illustrated in Figure 2e, we found that slight Cl and W co-doping successfully increased the effective mass (m), which resulted in the turned "V" variation of the S (Figure 2b). The improved m could be explained by the change of band structure after W doping as shown in Figure 2f and Figure S5, Supporting Information. The Fermi energy moves into the conduction band and the total density of states (TDOS) increase near the conduction band edge (pointed by the red arrow) that contributes to the increase of m.
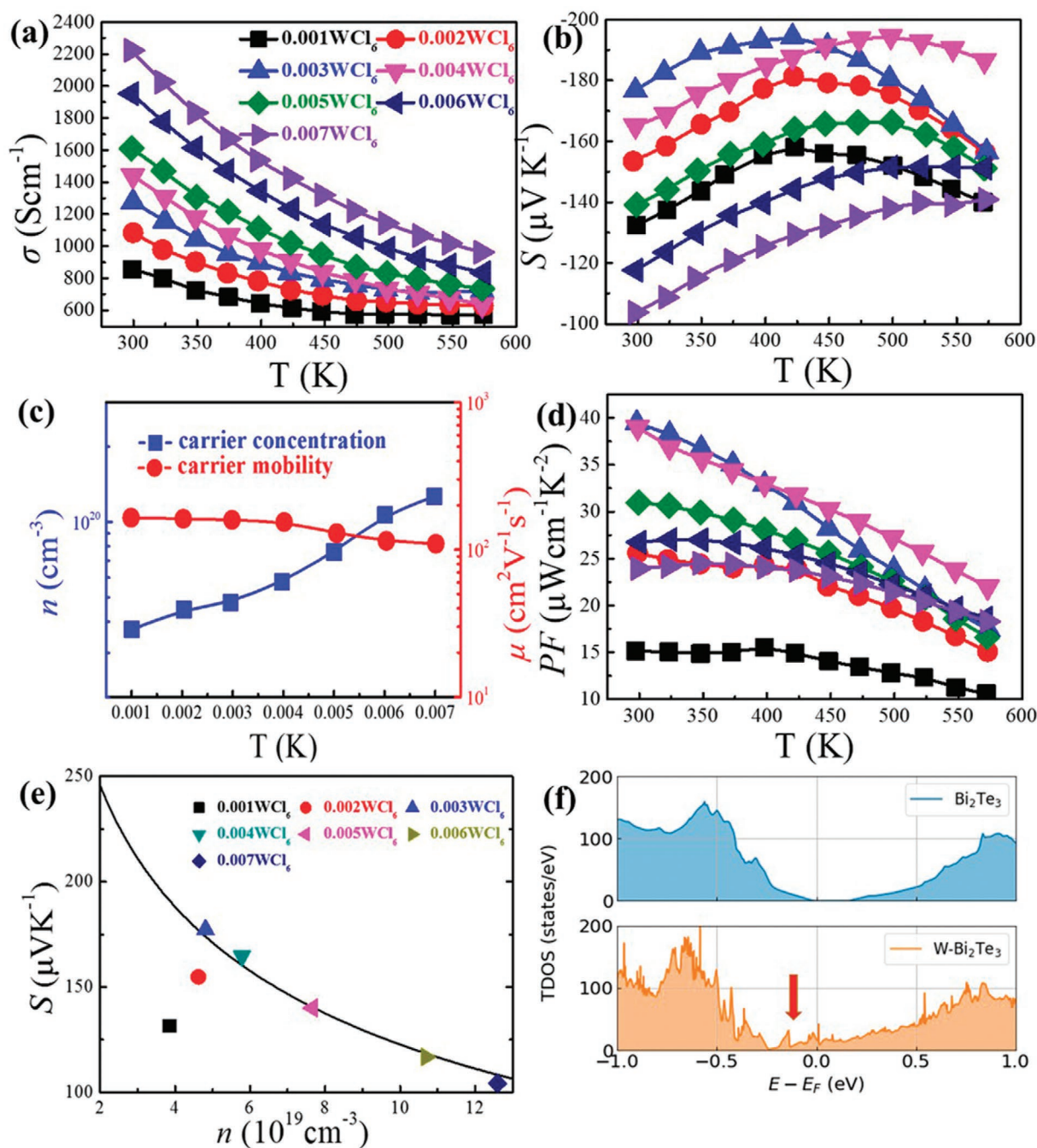
Figure 2. a) σ, b) S, c) n and μ, d) power factor (PF), and e) Pisarenko plots of $Bi_{2-x}W_xTe_{2.5-6x}Cl_{6x}Se_{0.5}$ ($x = 0.001–0.007$) samples, f) the total density of states (TDOS) for Bi_2Te_3 and W-doped Bi_2Te_3, respectively.

Figure 3a shows the temperature dependence of the total thermal conductivity (κ). As the doping content increased, the total thermal conductivity decreases at first and then increased, which is an opposite trend to the S. As a result, the 0.004 sample had the lowest κ of 0.96 W m^{-1} K^{-1} at 400 K. The total κ could be described as $\kappa = \kappa_{el} + \kappa_{l} + \kappa_{b}$, where is κ_{el}, κ_{l}, and κ_{b} are electronic, lattice, and bipolar thermal conductivities, respectively. $\kappa_{el} = L\sigma T$, where L is the Lorenz number, as shown in Figure S6, Supporting Information.[13]

Thus, the $\kappa_{l} + \kappa_{b}$ value could be calculated and it decreased with the increased doping content over the entire temperature range (Figure 3b), due to the increased point defects and U-process phonon scattering. As a result, a low κ_{l} value of $\approx$0.31 W m^{-1} K^{-1} was obtained in the 0.004 sample at 400 K. Figure 3c shows the temperature dependence of the ZT value for all doped samples. The highest ZT value (1.35 at 425 K) was achieved in the 0.004 sample, because of the synergistic improved PF and significantly reduced κ_{l}. The repeatability
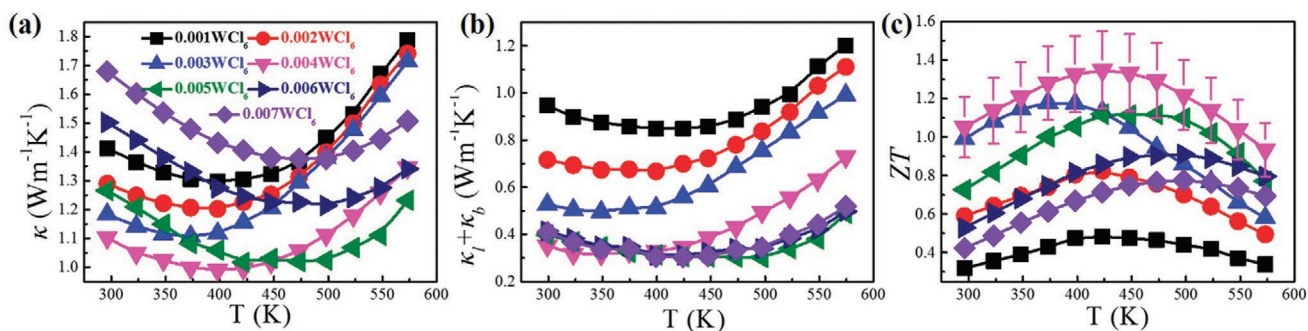
Figure 3. a) κ, b) $\kappa_i + \kappa_b$, and c) ZT value of $Bi_{2-x}W_xTe_{2.5-6x}Cl_{6x}Se_{0.5}$ ($x = 0.001–0.007$).

and round-robin test of the co-doped samples was confirmed, as shown in Figure S7, Supporting Information.

The aberration-corrected high angle annular dark field-scanning transmission electron microscope (HAADF-STEM) was employed to investigate the microstructure and atomic structure in un-doped and 0.004 WCl_6 samples. The un-doped sample exhibited relatively clean contrast and a typical Bi_2Te_3-based atomic structure (Figure S8a,b, Supporting Information).

The high density of dislocation was also observed in both un-doped and 0.004 WCl_6 samples (Figure S9, Supporting Information), which is a common structure in advanced Bi_2Te_3-based alloys for medium phonons scattering. Interestingly, a unique defect corresponding to the brighter linear structure was found in the 0.004 specimen, as highlighted by red arrows in **Figure** 4a,b. High-magnification STEM further indicates that this unique defective structure originates from additional
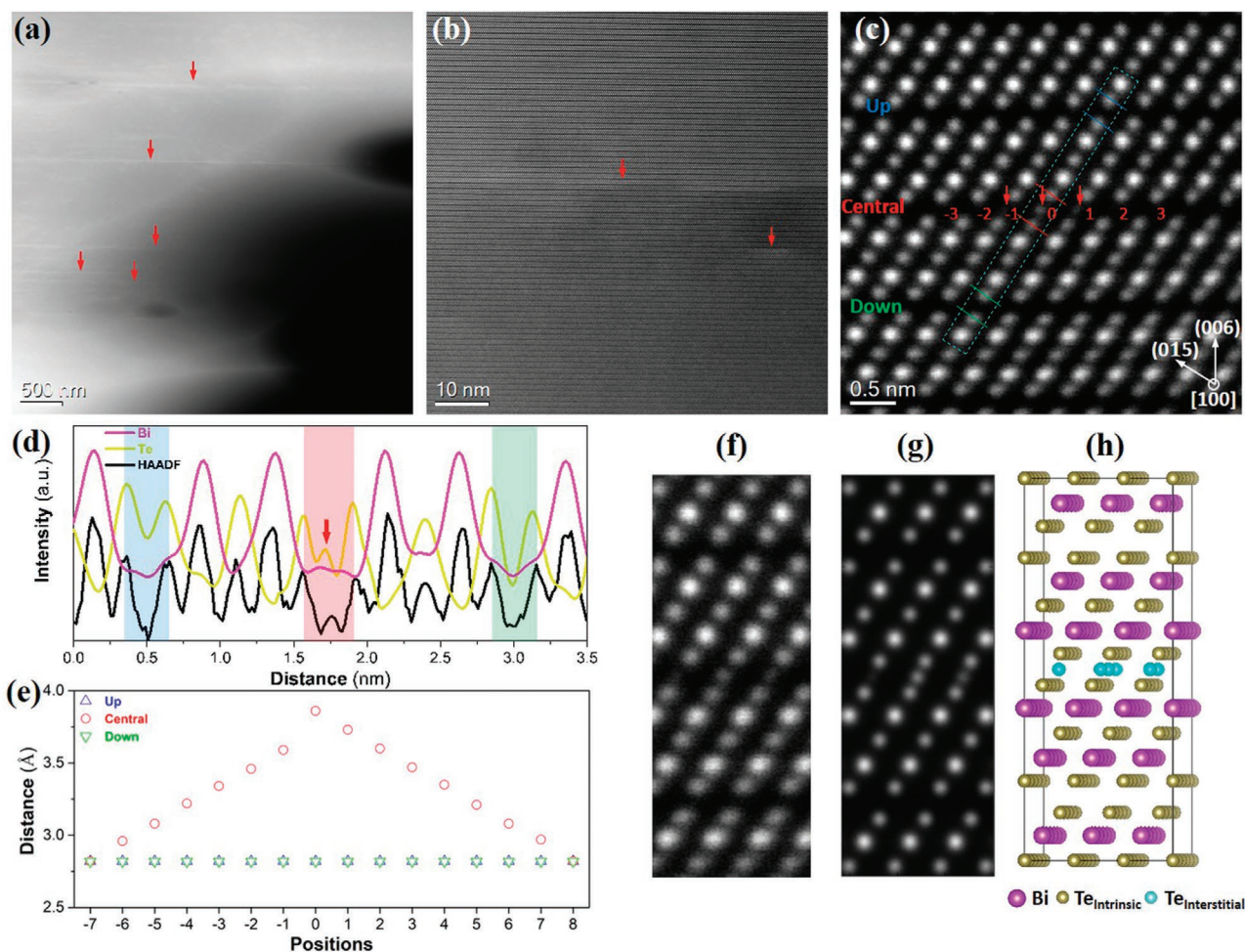
Figure 4. a) Microstructure and b,c) atomic structure of $Bi_{1.996}W_{0.004}Te_{2.476}Cl_{0.024}Se_{0.5}$ revealed by HAADF-STEM, d) EDX line profile of highlighted rectangle in (c), e) statistical analysis of Te–Te atom distances between adjacent van der Waals gap with and without interstitial atoms marked in (c), f–h) experimental STEM, simulated STEM, and corresponding potential atom model for the unique defect in the gap.

ADVANCED
SCIENCE NEWS
www.advancedsciencenews.com

NANO · MICRO
small
www.small-journal.com

atoms (highlighted by red arrows in Figure 4c) inserted into the van der Waals gap, where interstitial atoms in the gap observed in other regions unambiguously prove that the unique defect is a universal architecture in this sample (Figure S10, Supporting Information). Moreover, atomic-resolution energy dispersive X-ray spectroscopy (EDS) mapping (Figure S11, Supporting Information) and elemental intensity profiling (Figure 4d) were applied to reveal the nature of these additional atoms in the gap. Bi and Te signals fit well to the brighter and darker dots of Bi_2Te_3-based atomic structure in Figure 4c, and there are non-segregated signals for W and Cl elements. However, it should note that additional Te signal was found in the gap with interstitial atoms (light-red area in Figure 4d), as compared to no signal in the natural van der Waals gap (light-blue and light-green areas in Figure 4d). In addition, the DFT calculation results also prove the lowest energy characteristic of Te interstitial atom (Figure S9, Supporting Information). Since the contrast of HAADF-STEM is roughly proportional to the square of the atomic number (Z^2), STEM image simulation was performed to better understand this unique defect, with interstitial Te atoms in the gap. By comparing the intensity of intrinsic and interstitial Te atoms in experimental and simulated STEM images (Figure 4f,g), we found that interstitial Te atom columns from left to right were around 1/5, 3/5, and 2/5 filled (Figure S12, Supporting Information), indicating a partial filling of interstitial Te atoms along the depth of the gap as illustrated in the potential atom model (Figure 4h). Another interesting feature of the unique defect was also revealed by the statistical analysis of Te–Te atom distances between adjacent van der Waals gaps with and without interstitial atoms, as shown in Figure 4e. The three interstitial atoms could induce an apparent expansion of the gap distance, and the effect further extended to neighboring atoms, resulting in a several nanometers expansion in the gap, compared to no expansion of up and down gaps. This structure could weaken the relation between the layers and thus strongly enhance anharmonicity of TE material.

To understand the relationship between this unique defective structure and κ_l, the traditional Debye–Callaway model was calculated and here, the relaxation times including Umclapp scattering (τ_U), grain boundary scattering (τ_{GB}), Se substituted Te (τ_{PD-Se}), W substituted Bi (τ_{PD-W}), and Cl substituted Te (τ_{PD-Cl}) point defect scattering, cation vacancy point defect scattering (τ_V), and interstitial Te atom point defect (τ_{in-Te}) were considered.[14] These different phonon scattering mechanisms work together, resulting in low κ_l (Figure 3b). The details of the calculations and parameters are shown in the supporting information. There are three main phonon scattering mechanisms in this work (**Figure 5**b). At first, with increasing co-doping content, the transverse sound speed gradually decreased, while the longitude sound speed remained almost unchanged. This led to a huge increase in the Grüneisen parameter, as shown in Figure 5a, which indicates enhanced lattice anharmonic mechanics. This enhanced lattice anharmonicity is attributed to the enlarged apparent expansion of the gap distance (Figure 4). As a result, U process was significantly enhanced, compared to the single crystals shown in Figure 5b. In addition, the high density of dislocations (as depicted in Figure S8, Supporting Information) could also contribute significantly to the lowering of κ_l, and this phenomenon is also reported by different

studies regarding advanced Bi_2Te_3-based alloys. Finally, the unique interstitial Te atoms were observed for the first time in Bi_2Te_3-based alloys, and they are characterized as a kind of point defect. Point-defect scattering arises from an atomic size disorder in alloys. The disorder is described in terms of the scattering parameter (Γ) within the τ_{PD} formula as
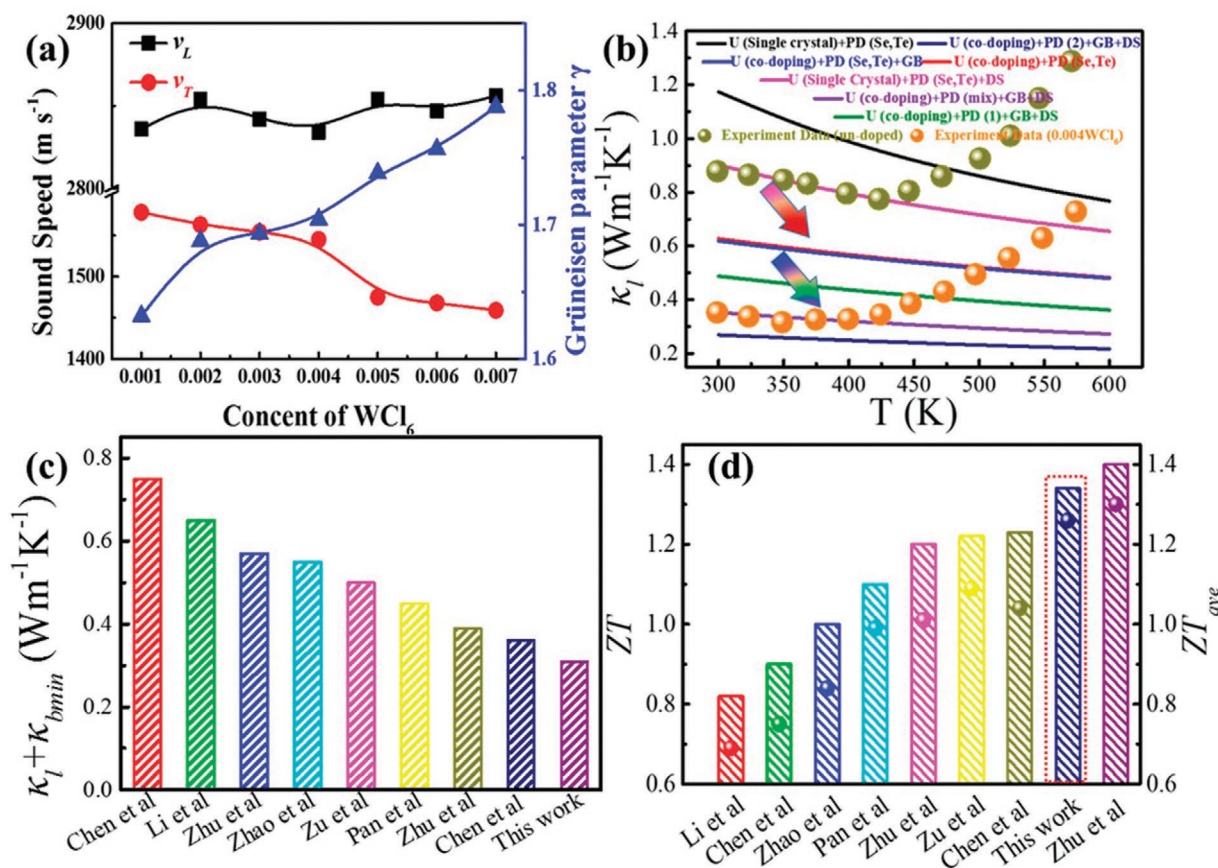
$$\tau_{PD}^{-1} = \frac{V\omega^4}{4\pi v_s^3}\Gamma \tag{1}$$

For the $Bi_{1.996}W_{0.004}Te_{2.476}Cl_{0.024}Se_{0.5}$ sample, W and Bi, and Cl and Te were substituted for each other; there were four crystallographic sites, including the sites of (W, Bi), (Cl, Te), interstitial Te atoms and Te vacancy V_{Te}. Additionally, some of the Te atoms in this study seem to generate inter-site atoms in the van der Waals gap, as shown in Figure 4c. Therefore, we separately calculated the contribution of each substitution, vacancy and inter-site atoms. First, we assumed the $Bi_{1.996}W_{0.004}Te_{2.476}Cl_{0.024}Se_{0.5}$ alloy only forms W_{Bi}-Cl_{Te} point defects, meaning no interstitial Te atoms or Te vacancies. Then, the theoretical κ_l values of this alloy were calculated for the entire temperature range, according to the Callaway model, in which the phonon scattering from U (co-doping)+GB+DS processes and W_{Bi}-Cl_{Te} point defects were considered (U(co-doping)+GB+DS + PD(1)). The results are plotted as a green line in Figure 5b. The experimental κ_l values are well below this green line across the entire temperature range, which indicates the W_{Bi}-Cl_{Te} point defects scattering phonons could not explain the low κ_l values in this work. Therefore, we assumed all the Te atoms, substituted by Cl atoms, entered into the van der Waals gap. We took the phonon scattering from U (co-doping)+GB+DS processes, W_{Bi}-Cl_{Te} point defects and interstitial Te atoms accompanied by Te vacancies (PD (2)) into account to calculate the theoretical κ_l values, and these values are plotted as a dark purple line in Figure 5b. After plotting the two theoretical lines (green and dark purple lines) in Figure 5b, we thought the interstitial Te atoms could explain the rapid decrease in κ_l of $Bi_{1.996}W_{0.004}Te_{2.476}Cl_{0.024}Se_{0.5}$ sample. The calculated κ_l values (dark purple line) that are lower than the experimental κ_l (orange dot) indicate only some of the substituted Te atoms enter into the van der Waals gap. Based on this idea, we fitted κ_l of $Bi_{1.996}W_{0.004}Te_{2.476}Cl_{0.024}Se_{0.5}$ (U(co-doping)+GB+DS+PD (mix)) in the entire measured temperature range, as shown by the purple line in Figure 5b. The experimental κ_l values of the $Bi_{1.996}W_{0.004}Te_{2.476}Cl_{0.024}Se_{0.5}$ sample can be explained by the Callaway model in the entire temperature range. A lowest κ_l of about 0.31 W m^{-1} K^{-1} at 350 K was obtained.

3. Conclusion

$Bi_{2-x}W_xTe_{2.5-6x}Cl_{6x}Se_{0.5}$ ($0.001 \leq x \leq 0.007$) bulk samples were fabricated using a traditional and easy melting process, in combination with spark plasma sintering. For thermal conductivity, the interstitial atoms induced by the W and Cl co-doping in this work not only scatter high frequency phonons as a kind of point defect, but also enhance anharmonicity due to enlarged van der Waals gap for whole frequency phonons scatter. As a result, a low κ_l of 0.31 W m^{-1} K^{-1} was obtained in the $Bi_{1.996}W_{0.004}Te_{2.476}Cl_{0.024}Se_{0.5}$

ADVANCED
SCIENCE NEWS

www.advancedsciencenews.com

NANO · MICRO

small

www.small-journal.com

Figure 5. a) Transverse, longitude sound speed (v_T and v_L) and Grüneisen parameter of $Bi_{2-x}W_xTe_{2.5-6x}Cl_{6x}Se_{0.5}$ ($x = 0.001$–0.007). b) Calculated in-plane lattice thermal conductivity of $Bi_{1.996}W_{0.004}Te_{2.476}Cl_{0.024}Se_{0.5}$, c) reported $\kappa_l + \kappa_{bmin}$ values, d) peak and average ZT of n-type Bi_2Te_3-based alloys.

sample, which is almost a 70% reduction compared to zone-melted ingot. The power factor was also improved due to the optimized carrier concentration and effective mass by this co-doping, which is confirmed by DFT calculation. Consequently, a high maximum and average ZT over 1.3 and 1.2, respectively, was achieved in $Bi_{1.996}W_{0.004}Te_{2.476}Cl_{0.024}Se_{0.5}$ sample at temperatures of 300–575 K, which is higher than most of the reported n-type Bi_2Te_3-based bulk material. A TE power generation module of this n-type material and homemade p-type Bi_2Te_3 sample produced a high efficiency (over 6%) at a temperature gradient of 235 K. This represents about 71% improvement, compared with a commercial zone-melt Bi_2Te_3-based module. This work has illustrated that an easy point-defect engineering methodology is highly effective for decreasing κ_l.

4. Experimental Section

The high-purity elements Bi, Te, Se (99.999%), and compound WCl_6 (99.9%) were weighed according to the stoichiometry of $Bi_{2-x}W_xTe_{2.5-6x}Cl_{6x}Se_{0.5}$ ($x = 0.001$–0.007). Subsequently, the mixtures were sealed in evacuated quartz ampoules ($\approx 10^{-4}$ Pa). First, the ampoules were heated to 773 K within 250 min and then held 120 min. Second, the ampoules were further heated to 1223 K at a speed of 1 K min^{-1} and remained 180 min, and finally cooled in the furnace. The obtained ingots were ground to powders by hands and followed to be sintered by SPS

under 50 MPa in an Ø10-mm graphite mold at 723 K for 5 min. Bar-shaped samples with dimensions of $2 \times 2 \times 10$ mm^3 were used for Seebeck and electrical conductivity measurements. Square with dimensions of $6 \times 6 \times 1.5$ mm^3, were utilized for thermal diffusivity (D) measurements. The specimens with dimensions of $4 \times 4 \times 0.8$ mm^3 were cut from the identical plates for Hall coefficient measurements. TE module with a dimension of $25 \times 19 \times 3.1$ mm^3 (24 n-p legs) were fabricated. Its power outputs and TE conversion efficiencies were evaluated by using commercial PEM-2 testing system (ULVAC-RIKO, Inc.).

The details of structure characterization (XRD, TEM), physical properties measurement (Hall measurement, Seebeck coefficient, electrical, and thermal conductivity), and TE module fabrication process could be found in the authors' previous work.[11e] In TE module, the TE properties of p-type samples are shown in the Figure S13, Supporting Information. The sound velocities were measured at 298 K by the ultrasonic pulse-echo method using an Olympus 5073PR pulser/receiver. The echoes were received by a 5 MHz transducer and displayed on a Tektronix MDO3054 digital oscilloscope.

First-principles calculations were carried out based on the density functional theory using the Vienna ab initio simulation package (VASP) with the projector augmented wave (PAW) method.[15] The exchange–correlation interactions were calculated by the generalized gradient approximation (GGA) of Perdew–Burke–Ernzerhof (PBE).[16] A cuboid-like pristine supercell containing 60 atoms was constructed to calculate the defect formation energy after a fully relaxation. Atomic relaxation was performed in the defective supercell with the lattice constant fixed. The atoms were relaxed until the total energy converged within 10^{-5} eV and the force converged in 0.01 eV Å^{-1}. Self-consistent calculations were performed with an energy cutoff of 350 eV, an energy convergence

**ADVANCED
SCIENCE NEWS**

www.advancedsciencenews.com

**NANO · MICRO
small**

www.small-journal.com

criterion of 10^{-5} eV, and a k-point spacing of $2\pi \times 0.027$ Å^{-1} using the Γ-centered Monkhorst–Pack scheme.[17] Experimental band gap of 0.18 eV was used. The defect formation energy E_f of a defect A_B (atom A on host site B) with a charge state q was defined according to the equation:

$$E_f\left(A_B^q, E_F\right) = E_{tot}\left(A_B^q\right) - E_{tot}(bulk) + \mu_B - \mu_A + q(E_V + E_F) + E_{FNV} \qquad (2)$$

where $E_{tot}(A_B^q)$ and $E_{tot}(bulk)$ are the total energies of the supercell with defect A_B^q and the perfect supercell, respectively; E_V, E_F, and E_{FNV} are the valence band maximum (VBM) energy of perfect supercell, the Fermi energy relative to the VBM, and the FNV correction,[18] respectively. μ_i is the chemical potential of element i, which is determined by $\mu_i = \mu_i^0 + \Delta\mu$, where μ_i^0 is the standard chemical potential of constituent i and $\Delta\mu$ is the deviation from the standard chemical potential, which reflects the growth condition. In this study, the formation energy of W_{Bi}, W_i, and Te_i under Bi-rich condition was calculated, where μ_{Bi} is the energy for a single Bi atom in the bulk phase. Three inequivalent interstitial sites were considered as shown in Figure S14, Supporting Information. The density of states (DOS) was calculated based on a $3 \times 3 \times 1$ supercell containing 135 atoms, with one Bi atom substituted by W. The atomic structure was fully relaxed with van der Waals correction (DFT-D3 with Becke–Johnson damping) and spin-orbit coupling was considered.

The effective band structures were calculated based on a $3 \times 3 \times 2$ supercell containing 60 atoms, as shown in Figure S15, Supporting Information. One Bi atom was substituted by W atom to study the effects of W on the electronic structure. The ionic positions were relaxed while the supercell lattice was kept fixed for the band unfolding technique.[19] Spin orbit coupling was not included in the effective band structure calculation.

Supporting Information

Supporting Information is available from the Wiley Online Library or from the author.

Conflict of Interest

The authors declare no conflict of interest.

Data Availability Statement

Research data are not shared.

[1] a) J. Yang, H.-L. Yip, A. K. Y. Jen, *Adv. Energy Mater.* **2013**, *3*, 549; b) M. Zebarjadi, K. Esfarjani, M. S. Dresselhaus, Z. F. Ren, G. Chen, *Energy Environ. Sci.* **2012**, *5*, 5147.

[2] a) L. D. Zhao, G. Tan, S. Hao, J. He, Y. Pei, H. Chi, H. Wang, S. Gong, H. Xu, V. P. David, C. Uher, G. J. Snyder, C. Wolverton, M. G. Kanatzidis, *Science* **2016**, *351*, 141;. b) L. D. Zhao, S. H. Lo, Y. Zhang, H. Sun, G. Tan, C. Uher, C. Wolverton, V. P. Dravid, M. G. Kanatzidis, *Nature* **2014**, *508*, 373.

[3] X. Xu, L. Xie, Q. Lou, D. Wu, J. He, *Adv. Sci.* **2018**, *5*, 1801514.

[4] a) J. Shuai, J. Mao, S. Song, Q. Zhu, J. Sun, Y. Wang, R. He, J. Zhou, G. Chen, D. J. Singh, Z. Ren, *Energy Environ. Sci.* **2017**, *10*, 799; b) B. Jiang, Y. Yu, J. Cui, X. Liu, L. Xie, J. Liao, Q. Zhang, Y. Huang, S. Ning, B. Jia1, B. Zhu, S. Bai, L. Chen, S. J. Pennycook, J. He, *Science* **2021**, *371*, 830.

[5] S. I. Kim, K. H. Lee, H. A. Mun, H. S. Kim, S. W. Hwang, J. W. Roh, D. J. Yang, W. H. Shin, X. S. Li, Y. H. Lee, G. J. Snyder, S. W. Kim, *Science* **2015**, *348*, 109.

[6] a) Y. Yu, D.-S. He, S. Zhang, O. Cojocaru-Mirédin, T. Schwarz, A. Stoffers, X.-Y. Wang, S. Zheng, B. Zhu, C. Scheu, D. Wu, J.-Q. He, M. Wuttig, Z.-Y. Huang, F.-Q. Zu, *Nano Energy* **2017**, *37*, 203; b) J. Li, Q. Tan, J.-F. Li, D.-W. Liu, F. Li, Z.-Y. Li, M. Zou, K. Wang, *Adv. Funct. Mater.* **2013**, *23*, 4317; c) Y. Zheng, Q. Zhang, X. Su, H. Xie, S. Shu, T. Chen, G. Tan, Y. Yan, X. Tang, C. Uher, G. J. Snyder, *Adv. Energy Mater.* **2015**, *5*, 1401391; d) Y. Pan, Y. Qiu, I. Witting, L. Zhang, C. Fu, J.-W. Li, Y. Huang, F.-H. Sun, J. He, G. J. Snyder, C. Felser, J.-F. Li, *Energy Environ. Sci.* **2019**, *12*, 624.

[7] M. U. Muzaffar, B. Zhu, Q. Yang, Y. Zhou, S. Zhang, Z. Zhang, J. He, *Mater. Today Phys.* **2019**, *9*, 100130.

[8] a) L. P. Hu, T. J. Zhu, X. Q. Yue, X. H. Liu, Y. G. Wang, Z. J. Xu, X. B. Zhao, *Acta Mater.* **2015**, *85*, 270; b) Y. Luo, J. Yang, Q. Jiang, W. Li, D. Zhang, Z. Zhou, Y. Cheng, Y. Ren, X. He, *Acta Mater.* **2017**, *127*, 185; c) F. Hao, P. Qiu, Y. Tang, S. Bai, T. Xing, H.-S. Chu, Q. Zhang, P. Lu, T. Zhang, D. Ren, J. Chen, X. Shi, L. Chen, *Energy Environ. Sci.* **2016**, *9*, 3120; d) R. Deng, X. Su, S. Hao, Z. Zheng, M. Zhang, H. Xie, W. Liu, Y. Yan, C. M. Wolverton, C. Uher, M. Kanatzidis, X. Tang, *Energy Environ. Sci.* **2018**, *11*, 1520.

[9] a) L. Hu, H. Wu, T. Zhu, C. Fu, J. He, P. Ying, X. Zhao, *Adv. Energy Mater.* **2015**, *5*, 1500411; b) M. Hong, T. C. Chasapis, Z. G. Chen, L. Yang, M. G. Kanatzidis, G. J. Snyder, J. Zou, *ACS Nano* **2016**, *10*, 4719;. c) B. Zhu, Z.-Y. Huang, X.-Y. Wang, Y. Yu, L. Yang, N. Gao, Z.-G. Chen, F.-Q. Zu, *Nano Energy* **2017**, *42*, 8.

[10] a) H.-M. Wu, S.-A. Chen, *Synth. Met.* **1987**, *20*, 169; b) K.-Q. T. Toshio Masuda, N. Sasaki, T. Higashimura, *Macromolecules* **1976**, *9*, 661.

[11] a) J. Jiang, L. Chen, Q. Yao, S. Bai, Q. Wang, *Mater. Chem. Phys.* **2005**, *92*, 39; b) Y. Pan, T.-R. Wei, C.-F. Wu, J.-F. Li, *J. Mater. Chem. C* **2015**, *3*, 10583; c) L. P. Hu, X. H. Liu, H. H. Xie, J. J. Shen, T. J. Zhu, X. B. Zhao, *Acta Mater.* **2012**, *60*, 4431; d) Y. Pan, J.-F. Li, *NPG Asia Mater.* **2016**, *8*, e275; e) B. Zhu, X. Liu, Q. Wang, Y. Qiu, Z. Shu, Z. Guo, Y. Tong, J. Cui, M. Gu, J. He, *Energy Environ. Sci.* **2020**, *13*, 2106.

[12] a) S. Wang, W. Xie, H. Li, X. Tang, *Intermetallics* **2011**, *19*, 1024; b) X. Hu, K. Nagase, P. Jood, M. Ohta, A. Yamamoto, *J. Electron. Mater.* **2015**, *44*, 1785.

[13] B. Jiang, X. Liu, Q. Wang, J. Cui, B. Jia, Y. Zhu, J. Feng, Y. Qiu, M. Gu, Z. Ge, J. He, *Energy Environ. Sci.* **2020**, *13*, 579.

[14] J. He, M. G. Kanatzidis, V. P. Dravid, *Mater. Today* **2013**, *16*, 166.

[15] G. Kresse, J. Furthmüller, *Phys. Rev. B* **1996**, *54*, 11169.

[16] J. P. Perdew, K. Burke, M. Ernzerhof, *Phys. Rev. Lett.* **1996**, *77*, 3865.

[17] H. J. Monkhorst, J. D. Pack, *Phys. Rev. B* **1976**, *13*, 5188.

[18] C. Freysoldt, J. Neugebauer, C. G. Van de Walle, *Phys. Rev. Lett.* **2009**, *102*, 016402.

[19] V. Popescu, A. Zunger, *Phys. Rev. B* **2012**, *85*, 085201.